Ab initio electron-lattice downfolding: Potential energy landscapes, anharmonicity, and molecular dynamics in charge density wave materials

Arne Schobert[1,2,3], Jan Berges[2,4], Erik G. C. P. van Loon[5], Michael A. Sentef[1,2,6,7], Sergey Brener[3], Mariana Rossi[6*] and Tim O. Wehling[3,8†]

1 Institut für Theoretische Physik, Universität Bremen, D-28359 Bremen, Germany
2 Bremen Center for Computational Materials Science and MAPEX Center for Materials and Processes, Universität Bremen, D-28359 Bremen, Germany
3 I. Institute of Theoretical Physics, Universität Hamburg, D-22607 Hamburg, Germany
4 U. Bremen Excellence Chair, Universität Bremen, D-28359 Bremen, Germany
5 NanoLund and Division of Mathematical Physics, Department of Physics, Lund University, SE-22100 Lund, Sweden
6 Max Planck Institute for the Structure and Dynamics of Matter, Center for Free Electron Laser Science (CFEL), D-22761 Hamburg, Germany
7 H. H. Wills Physics Laboratory, University of Bristol, Bristol BS8 1TL, United Kingdom
8 The Hamburg Centre for Ultrafast Imaging, D-22761 Hamburg, Germany

⋆ mariana.rossi@mpsd.mpg.de , † tim.wehling@uni-hamburg.de

Abstract

The interplay of electronic and nuclear degrees of freedom presents an outstanding problem in condensed matter physics and chemistry. Computational challenges arise especially for large systems, long time scales, in nonequilibrium, or in systems with strong correlations. In this work, we show how downfolding approaches facilitate complexity reduction on the electronic side and thereby boost the simulation of electronic properties and nuclear motion—in particular molecular dynamics (MD) simulations. Three different downfolding strategies based on constraining, unscreening, and combinations thereof are benchmarked against full density functional calculations for selected charge density wave (CDW) systems, namely $1H\text{-}TaS_2$, $1T\text{-}TiSe_2$, $1H\text{-}NbS_2$, and a one-dimensional carbon chain. We find that the downfolded models can reproduce potential energy surfaces on supercells accurately and facilitate computational speedup in MD simulations by about five orders of magnitude in comparison to purely *ab initio* calculations. For monolayer $1H\text{-}TaS_2$ we report classical and path integral replica exchange MD simulations, revealing the impact of thermal and quantum fluctuations on the CDW transition.

Contents

1 Introduction

The coupling of electronic and nuclear degrees of freedom is an extremely complex problem of relevance to multiple branches of the natural sciences, ranging from quantum materials in and out of thermal equilibrium [1–6] to chemical reaction dynamics [7,8]. Long-standing problems include the simulation of coupled electronic and nuclear degrees of freedom for large systems and large time scales, in excited states of matter or systems with strong electronic correlations. A central contributor to these challenges is the complexity of first-principles treatments of the electronic subsystem usually required to address real materials.

Charge density wave (CDW) materials exemplify these challenges. The bidirectional coupling between electrons and nuclei results in a phase transition, where the atoms of the CDW material acquire a periodic displacement from a high-temperature symmetric structure [1,3,9]. Understanding the characteristics of the CDW phase transitions, the emergence of collective CDW excitations, the control of CDW states, and excitation induced dynamics of CDW systems [10–19] requires typically simulations on supercells involving several hundred or thousand atoms, where eV-scale electronic processes intertwine with collective mode dynamics at the meV scale. CDW systems thus define a formidable spatio-temporal multiscale problem. Solutions to this problem can be attempted with variational techniques [20–24], which neglect certain anharmonic effects like the anharmonic phonon decay, or by trying to circumvent the multi-scale problem by scale-separation [25, 26].

Corresponding complexity reduction strategies have been developed in distinct fields: Multi-scale coarse-grained models, machine-learning models [27–31], or (density functional) tight binding potentials [32–53] have been put forward. In these methods, models are defined by fitting semiempirical or "machine learned" (neural networks, Gaussian processes, others) parameter functions to reference data often taken from density-functional theory (DFT) [54] calculations.

In the field of strongly correlated electrons, one also deals with minimal models, which typically focus on low-energy degrees of freedom: The electronic system is divided into high- and low-energy sectors. Then, the high-energy states are integrated out via field theoretical or perturbative means, leaving an effective low-energy model [55]. Methods for the derivation of model parameters include the constrained random phase approximation (cRPA) [56–62], constrained density functional perturbation theory (cDFPT) [63–67], and the constrained functional renormalization group [68–70]. The field theoretical integrating out of certain electronic states is often called "downfolding".

In this work, we demonstrate how downfolding approaches for complexity reduction on the electronic side boost the simulation of coupled electronic and nuclear degrees of freedom—in particular molecular dynamics (MD) simulations. The idea is to map the first-principles solid-state Hamiltonian onto minimal quantum lattice models, where "minimal" refers to the dimension of the single-particle Hilbert space. Three different downfolding strategies based on constraining, unscreening, and combinations thereof, are compared and demonstrated along example cases from the domain of CDW materials.

We start by introducing the first-principles electron-nuclear Hamiltonian and the minimal quantum lattice models together with the three downfolding schemes in Section 2. Potential energy surfaces resulting from the downfolded models are benchmarked against DFT for exemplary CDW systems in Section 3. MD simulations based on a downfolded model are presented in Section 4, where the CDW transition of $1H\text{-}TaS_2$ is studied as a function of temperature, and the computational performance gain from downfolding is analyzed.

2 From first-principles to minimal lattice models

The general Hamiltonian of interacting electrons and nuclei in the position representation and atomic units, where in particular $m_e = e = 1$, reads

$$H_{\text{FP}} = -\sum_i \frac{\Delta_i}{2} - \sum_k \frac{\Delta_k}{2M_k} + \sum_{i<j} \frac{1}{|r_i - r_j|} + \sum_{k<l} \frac{Z_k Z_l}{|R_k - R_l|} - \sum_{ik} \frac{Z_k}{|r_i - R_k|}, \quad (1)$$

where r_i and R_k are electronic and nuclear positions, Δ_i and Δ_k are the corresponding Laplace operators, and Z_k and M_k are atomic numbers and nuclear masses. This Hamiltonian is also called "first-principles (FP) Hamiltonian", since only fundamental laws (i.e., the Schrödinger equation, Coulomb potential, etc.) and fundamental constants (elementary charges etc.) enter. It accounts for full atomic scale and chemical details. Numerical treatments leading directly from this Hamiltonian to physical results are called "*ab initio*", cf. Fig. 1 (left).

In principle, DFT provides us with a tool to calculate the total (free) energy and forces given fixed atomic positions R_k as needed for MD simulations in the Born-Oppenheimer approximation [71]. However, DFT calculations with large supercells can become prohibitively expensive (cf. Fig. 7 for benchmark calculations later in this work). As a consequence, DFT simulations of phase transitions governed by inhomogeneity effects are often very challenging. It is, thus, desirable to obtain energies and forces in a cheaper way, while remaining close to the quantum mechanical accuracy of *ab initio* simulations.

First-principles Hamiltonian   **Minimal lattice model**

$$H_{\text{FP}} = -\sum_i \frac{\Delta_i}{2} - \sum_k \frac{\Delta_k}{2M_k} + \sum_{i<j} \frac{1}{|\boldsymbol{r}_i - \boldsymbol{r}_j|}$$
$$+ \sum_{k<l} \frac{Z_k Z_l}{|\boldsymbol{R}_k - \boldsymbol{R}_l|} - \sum_{ik} \frac{Z_k}{|\boldsymbol{r}_i - \boldsymbol{R}_k|}$$

$$H = \sum_{mn} (t_{mn} + \boldsymbol{u}\boldsymbol{d}_{mn}) c_m^\dagger c_n$$
$$+ \frac{1}{2} \boldsymbol{u}^T C \, \boldsymbol{u} - \mathcal{F}^0 \boldsymbol{u}$$

Downfolding

Full *ab initio*   **Model solving**
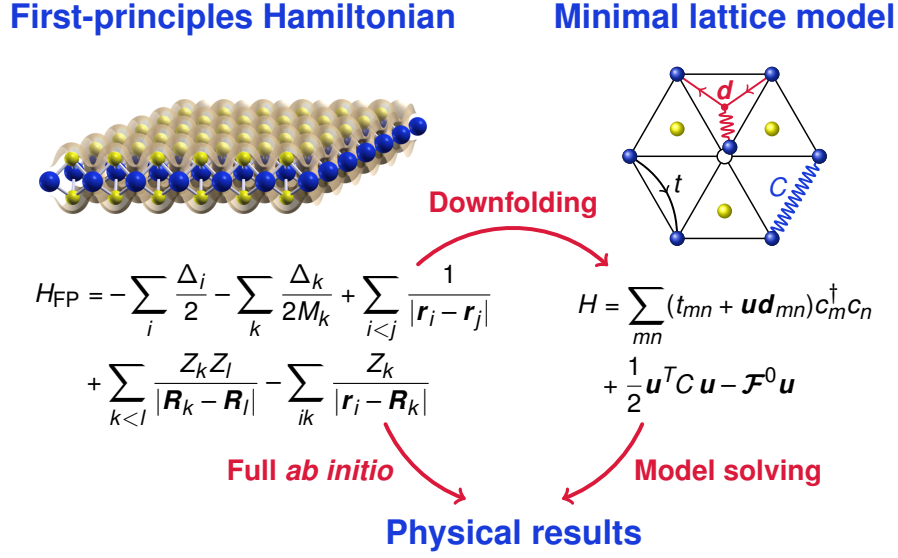
Physical results

Figure 1: *Ab initio* versus *ab initio* based downfolding approaches to coupled electron-nuclear dynamics.

Here, our goal is to use a reduced low-energy electronic Hilbert space for this purpose, with only a few orbitals per unit cell, cf. Fig. 1 (right).

We thus aim to work with a lattice model

$$H = H_{\text{el}} + H_{\text{n}} + H_{\text{el-n}}, \tag{2}$$

which consists of the low-energy electronic subsystem

$$H_{\text{el}} = H_{\text{el}}^0 + H_{\text{el}}^1 + H_{\text{DC}}, \tag{3}$$

with one-body

$$H_{\text{el}}^0 = \sum_{\boldsymbol{k}n} \varepsilon_{\boldsymbol{k}n}^0 c_{\boldsymbol{k}n}^\dagger c_{\boldsymbol{k}n}, \tag{4}$$

Coulomb interaction

$$H_{\text{el}}^1 = \frac{1}{2N} \sum U_{\boldsymbol{q}\boldsymbol{k}mn\boldsymbol{k}'m'n'} c_{\boldsymbol{k}+\boldsymbol{q}m}^\dagger c_{\boldsymbol{k}'n'}^\dagger c_{\boldsymbol{k}'+\boldsymbol{q}m'} c_{\boldsymbol{k}n}, \tag{5}$$

and double counting (H_{DC}) parts, the nuclear subsystem

$$H_{\text{n}} = -\sum_k \frac{\Delta_k}{2M_k} + V^0(\boldsymbol{u}_1, \ldots, \boldsymbol{u}_{N_{\text{n}}}), \tag{6}$$

and a coupling between the electronic and nuclear degrees of freedom

$$H_{\text{el-n}} = \sum_{\boldsymbol{q}\boldsymbol{k}mn} V_{\boldsymbol{q}\boldsymbol{k}mn}(\boldsymbol{u}_1, \ldots, \boldsymbol{u}_{N_{\text{n}}}) c_{\boldsymbol{k}+\boldsymbol{q}m}^\dagger c_{\boldsymbol{k}n}. \tag{7}$$

The electronic subspace is spanned by a set of low-energy single particle states $|\boldsymbol{k}n\rangle$, with $\boldsymbol{k}$ the crystal momentum, and n summarizing further quantum numbers (band index, spin). $c_{\boldsymbol{k}n}^\dagger$ ($c_{\boldsymbol{k}n}$) are the corresponding electronic creation (annihilation) operators. N is the number of $\boldsymbol{k}$ points summed over. The nuclear degrees of freedom are expressed in terms of displacements $(\boldsymbol{u}_1, \ldots, \boldsymbol{u}_{N_{\text{n}}}) \equiv \boldsymbol{u} = \boldsymbol{R} - \boldsymbol{R}_0$ from a relaxed reference structure $\boldsymbol{R}_0$.

H_{el} describes the low-energy electronic subsystem in the non-distorted configuration ($\boldsymbol{u}=0$) with the effective electronic dispersion $\varepsilon^0_{\boldsymbol{k}n}$ and an effective Coulomb interaction U. In this work, $\varepsilon^0_{\boldsymbol{k}n}$ is always taken from the DFT Kohn-Sham eigenvalues of the undistorted reference system. Whenever $U \neq 0$, a term H_{DC} has to be added to avoid double counting (DC) of the Coulomb interaction already contained in the Kohn-Sham eigenvalues (see Appendix A).

V^0 plays the role of an effective interaction between the nuclei, or equivalently a partially screened deformation energy, which accounts for the Coulomb interaction between the nuclei and the interaction between the nuclei and the high-energy electrons not accounted for in H_{el}. In this work, we expand V^0 to second order in the atomic displacements $\boldsymbol{u}$,

$$H_{\text{def}} = V^0 = -\sum_i \mathcal{F}^0_i u_i + \frac{1}{2}\sum_{ij} u_i C_{ij} u_j \,, \tag{8}$$

where $\mathcal{F}^0$ is a force vector and C a force constant matrix. The coupling between the displacements and the low-energy electronic system from Eq. (7) is expanded to first order in the displacements $\boldsymbol{u}$:

$$H_{\text{el-n}} = \boldsymbol{u}\sum_{\boldsymbol{q}\boldsymbol{k}mn}\boldsymbol{d}_{\boldsymbol{q}\boldsymbol{k}mn}c^\dagger_{\boldsymbol{k}+\boldsymbol{q}m}c_{\boldsymbol{k}n} \,. \tag{9}$$

Here, $\boldsymbol{d}_{\boldsymbol{q}\boldsymbol{k}mn} = \boldsymbol{\nabla}_{\boldsymbol{u}} V_{\boldsymbol{q}\boldsymbol{k}mn}(\boldsymbol{u})$, and $\boldsymbol{u} \cdot \boldsymbol{d}_{\boldsymbol{q}\boldsymbol{k}mn}$ plays the role of a displacement-induced potential acting on the low-energy electrons.

MD simulations are a major motivation for constructing the low-energy electronic model. These simulations are here performed at various temperatures, using an electronic model that is established based on a single DFT and density functional perturbation theory (DFPT) calculation. The effective free energy of the system at given nuclear coordinates $\boldsymbol{R} = \boldsymbol{R}_0 + \boldsymbol{u}$ is

$$F(\boldsymbol{u}) = -kT \log Z(\boldsymbol{u}) \,. \tag{10}$$

Here, the partition function $Z(\boldsymbol{u}) = \text{Tr}_{\text{el}} \exp(-\beta H)$ traces out the electronic degrees of freedom but not the nuclei. Thus, $F(\boldsymbol{u})$ plays the role of a potential energy surface, which governs the dynamics of the nuclei in Born-Oppenheimer approximation. Forces acting on the nuclei are then $\mathcal{F} = -\boldsymbol{\nabla}_{\boldsymbol{u}} F(\boldsymbol{u})$ and can be conveniently obtained using the Hellmann-Feynman theorem (see Appendix B):

$$\mathcal{F} = -\sum_{\boldsymbol{q}\boldsymbol{k}mn}\boldsymbol{d}_{\boldsymbol{q}\boldsymbol{k}mn}\langle c^\dagger_{\boldsymbol{k}+\boldsymbol{q}m}c_{\boldsymbol{k}n}\rangle \,. \tag{11}$$

C, U, and $\boldsymbol{d}$ entering the model Hamiltonian H are not bare but (partially) screened quantities. The (partial) screening has to account for electronic processes not contained explicitly in H. Here, we consider three different schemes to determine C, U, and $\boldsymbol{d}$:

Model I strictly follows the idea of the constrained theories [57, 64]. In these theories, the high-energy electronic degrees of freedom are integrated out to derive the low-energy model. The parameters entering the low-energy Hamiltonian are therefore "partially screened" by the high-energy electrons. In particular, we use cRPA for the Coulomb interaction U and cDFPT for the displacement-induced potential $\boldsymbol{d}$ and for the force constant matrix C.

Model II again applies U from cRPA. Now, however, $\boldsymbol{d}$ and C are based on the *unscreening* of the respective DFPT quantities using U inspired by Ref. [72].

Model III considers a non-interacting low-energy system, $U = 0$. $\boldsymbol{d}$ is taken from DFPT. C is obtained from unscreening DFPT. This approach is inspired by Ref. [73].

In all models, the force vector $\mathcal{F}^0$ entering H_{def} in Eq. (8) is chosen to guarantee that $dF/du_i|_{\boldsymbol{u}=0} = 0$, i.e., vanishing forces also in the models for the reference structure $\boldsymbol{R}_0$. The term $-\mathcal{F}^0\boldsymbol{u}$, thus, plays the role of a "force double counting correction" similar to Refs. [63,64].

Since the downfolding is done on the primitive unit cell for $\boldsymbol{u} = 0$, and we are interested in the potential energy surface for displacements on supercells, we have to map the model parameters ε^0, C, U, and $\boldsymbol{d}$ from the unit cell to the supercell. For displacements with the supercell periodicity, we can set $\boldsymbol{q} = 0$ in Eq. (9) and—within the random phase approximation (RPA)—also in Eq. (5) and drop the corresponding subscripts.

We have implemented this mapping for arbitrary commensurate supercells defined by their primitive lattice vectors $\boldsymbol{A}_i = \sum_j N_{ij}\boldsymbol{a}_j$ with integer N_{ij} [74]. It relies on localized representations in the basis of Wannier functions and atomic displacements [75], for which the mapping is essentially a relabeling of basis and lattice vectors.

2.1 Unscreening in models II and III

The central idea of models II and III is to choose C entering H_{def} such that $d^2F/du_i du_j|_{\boldsymbol{u}=0} = C_{ij}^{\text{DFT}}$, where the latter are the DFT force constants, accessible via DFPT. In model II we additionally require that the screened deformation-induced potential and accordingly the screened electron-phonon vertex at the level of the static RPA matches the corresponding DFPT quantity.

The unscreening procedure is represented diagrammatically: The Green's function resulting from the undistorted Kohn-Sham dispersion $\varepsilon_{\boldsymbol{k}n}^0$ is shown as a black arrow line, $G \rightarrow$ ———. We use a wavy line to denote the Coulomb interaction $U \rightarrow \sim\sim$ obtained from cRPA. The deformation-induced potential obtained from DFPT, which is by definition fully screened, is represented as a black dot, $\boldsymbol{d}^{\text{DFT}} = \boldsymbol{d}^{\text{III}} \rightarrow \bullet$.

2.1.1 Model II

We define the unscreened deformation-induced potential $\boldsymbol{d}^{\text{II}} \rightarrow \bullet$ (red dot) entering model II via Eq. (9) as

$$\textcolor{red}{\bullet} = \bullet - \sim\!\!\!\overbrace{}\!\!\!\bullet , \tag{12}$$

which can be written in shorthand notation as $d^{\text{II}} = d - U\Pi d$, or explicitly as

$$\boldsymbol{d}_{\boldsymbol{k}mn}^{\text{II}} = \boldsymbol{d}_{\boldsymbol{k}mn} - \frac{1}{N}\sum_{\boldsymbol{k}'m'n'\alpha\beta} \varphi_{\boldsymbol{k}\alpha m}^* \varphi_{\boldsymbol{k}\beta n} U_{\alpha\beta} \varphi_{\boldsymbol{k}'\alpha m'} \varphi_{\boldsymbol{k}'\beta n'}^* \frac{f(\varepsilon_{\boldsymbol{k}'m'}) - f(\varepsilon_{\boldsymbol{k}'n'})}{\varepsilon_{\boldsymbol{k}'m'} - \varepsilon_{\boldsymbol{k}'n'}} \boldsymbol{d}_{\boldsymbol{k}'m'n'} . \tag{13}$$

Here, $\varepsilon_{\boldsymbol{k}n}$, $\varphi_{\boldsymbol{k}\beta n}$ are the eigenvalue and -vector of band n from the undistorted Wannier Hamiltonian, and $U_{\alpha\beta}$ is the cRPA Coulomb interaction in the orbital basis.

The definition in Eq. (12) implies that the static RPA screening of the deformation-induced potential in model II indeed matches the DFPT input, since

$$\bullet = \textcolor{red}{\bullet} + \sim\!\!\!\overbrace{}\!\!\!\bullet$$
$$= \textcolor{red}{\bullet} + \sim\!\!\!\overbrace{}\!\!\!\textcolor{red}{\bullet} + \sim\!\!\!\overbrace{}\!\!\!\sim\!\!\!\overbrace{}\!\!\!\textcolor{red}{\bullet} + \ldots \tag{14}$$

The force constant matrix $C = C^{\text{DFT}} - \Delta C^{\text{RPA}}$ entering model II is obtained by unscreening the DFPT fully screened force constants C^{DFT} on the RPA level, i.e., we subtract the second-order response in RPA of the electronic system to the atomic displacements, as given by the bubble diagram

$$\Delta C^{\text{RPA}} = \bullet\!\!\!\overbrace{}\!\!\!\textcolor{red}{\bullet} . \tag{15}$$

Table 1: Comparison of downfolded models.

	Model I	Model II	Model III
Coulomb interaction [Eq. (5)]	cRPA	cRPA	—
Electron-phonon coupling[1] [Eq. (9)]	cDFPT	DFPT $(\star)^{*}$ ●	DFPT ●
Force constants [Eq. (8)]	cDFPT	DFPT $(\star)^{*}$	DFPT $(\star)^{*}$

[1] as in displacement-induced potential.

[*] $(\star)$ refers to *unscreened* quantities.

2.1.2 Model III

Again, we construct the total free energy to be exact in second order. As in model II, we have to subtract the unwanted second order, $C = C^{\text{DFT}} - \Delta C^{\text{III}}$. The change in the interatomic force constants for this non-interacting model is given by the bubble diagram (cf. Appendix B)

$$\Delta C^{\text{III}} = \text{⬤}\bigcirc\text{⬤}. \tag{16}$$

The unscreening is exact when the DFT force constants, the bubble diagram, and the free energy are evaluated at the same electronic temperature T_{DFT}. This electronic temperature facilitates the treatment of metals within DFT calculations. However, on the model side we have the freedom to evaluate the free energy at a different electronic temperature T_M. Interestingly, the resulting second order is still a very good approximation to the DFT force constants at temperature T_M [73,76], as it will be demonstrated in this work.

This completes the definitions of models I, II, and III, which are also summarized in Table 1. In the following, we will explain and demonstrate the downfolding according to models I–III along the example case of monolayer 1H-TaS$_2$.

3 CDW potential energy landscapes in 1H-TaS$_2$: DFT vs downfolding

Monolayer 1H-TaS$_2$ exhibits a 3×3 CDW [77–79], where atoms are displaced from their symmetric positions as illustrated in Fig. 2a. Coupling between electrons within the low-energy subspace (highlighted in Fig. 2b) and the lattice distortions $\boldsymbol{u}$ is responsible for the 3×3 CDW instability [66]. Hence, we choose these three bands to span the low-energy subspace of electrons in the Hamiltonian H.

We present practical calculations using downfolded models I–III and benchmark the resulting potential energy landscapes against full DFT calculations. Details of the DFT calculations are presented in Appendix C. The energy landscapes will be illustrated along the displacement direction of the CDW distortion: $\boldsymbol{u} = \alpha(\boldsymbol{R}_{\text{CDW}} - \boldsymbol{R}_0)$. Here, $\boldsymbol{R}_0$ is the symmetric relaxed structure, and $\boldsymbol{R}_{\text{CDW}}$ is the CDW structure as obtained by DFT. α plays the role of a scalar coordinate, where by construction $\alpha = 0$ yields the symmetric state and $\alpha = 1$ the CDW displacement pattern. Note, however, that the models readily yield the full energy landscape for arbitrary displacements.

Model I starts with partially screened force constants C from cDFPT in H_{def}, which exclude screening processes taking place within the low-energy electronic target space highlighted in Fig. 2b. The "bare" harmonic potential energy versus displacement curves resulting from H_{def} (dark gray cDFPT parabola) is compared to full DFT total energy calculations (crosses) in Fig. 2c. The upward opened cDFPT parabola shows that the CDW lattice instability is induced by the electrons of the target subspace, in accordance with Ref. [66].
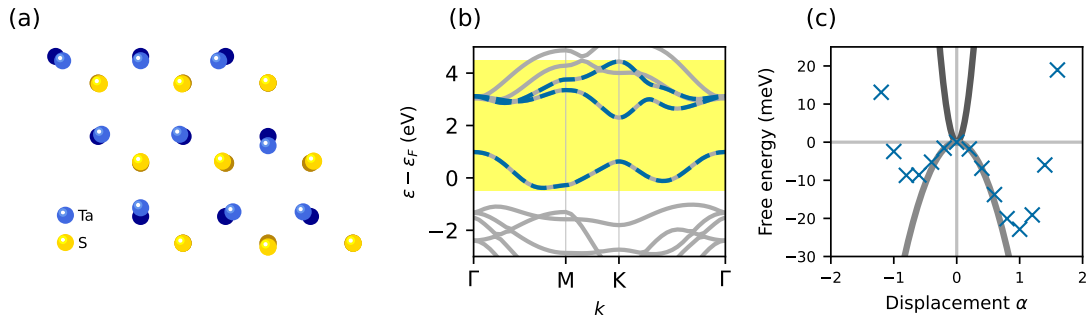
Figure 2: (a) Crystal structure of the 3×3 CDW in 1H-TaS$_2$ (displacements are increased by a factor of 5 for visibility). (b) Electronic bands of 1H-TaS$_2$ from DFT (gray) and Wannier bands (blue dashed), which span the cDFPT active subspace highlighted in yellow. (c) Born-Oppenheimer potential energy surface from DFT for the 3×3 CDW in 1H-TaS$_2$ (blue crosses). Its negative curvature matches the DFPT parabola (light gray curve). The cDFPT parabola, which is not screened by the active subspace electrons, is opened upward (dark gray curve).

We account for density-density type Coulomb matrix elements in H_{el}, which we obtain from cRPA, and solve the resulting model Hamiltonian H for the potential energy landscape $F(\boldsymbol{u})$ in Hartree approximation. See Appendix A for a detailed description of the Hartree calculations. The resulting total (free) energy versus displacement curve is compared to DFT in Fig. 3a. Model I generates an anharmonic double-well potential and thus features a CDW instability like DFT, which is qualitatively reproduced. Nevertheless, there is some deviation of model I from DFT, which originates mainly from the harmonic term. In comparison to DFT, model I and its subsequent Hartree solution involve two additional approximations, which could be responsible for the deviations to second order: neglecting non density-density type Coulomb terms, and neglecting exchange-correlation effects.

Model II suppresses deviations from the DFT potential energy landscape to second order in $\boldsymbol{u}$ by construction: Since the fully screened deformation energy from DFPT agrees with the DFT energy versus displacement curve (see Fig. 2b), as it must be, also the solution of the downfolded model II matches DFT to second order in the displacement (Fig. 3b). The overall match between the downfolded model II and DFT is clearly much better than for model I and indeed almost quantitative also at displacements $|\alpha| > 1$, where anharmonic terms are substantial.

Also **model III**, which involves non-interacting electrons coupled to lattice deformations via fully screened DFPT displacement-induced potentials, recovers the DFT potential energy vs displacement curve for the 3×3 CDW distortion in 1H-TaS$_2$ almost quantitatively (Fig. 3c) and even slightly better than model II.

We also applied downfolded model III to monolayer 1T-TiSe$_2$, a one-dimensional carbon chain, and monolayer 1H-NbS$_2$ as examples of further CDW materials. The resulting potential energy landscapes in Fig. 4 show the agreement between DFT and the downfolded model. Hence, model III captures the most important anharmonicities in these cases. CDWs are especially, but not exclusively, found in low-dimensional systems. As a consequence, we focussed on low-dimensional materials for this benchmark. However, the downfolding formalism is independent of dimensionality.
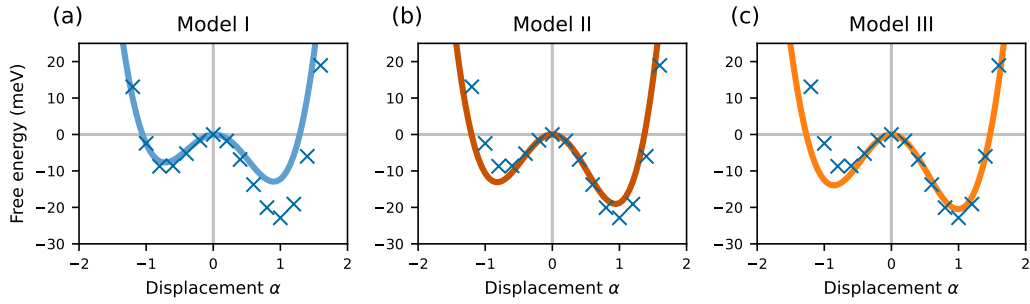
Figure 3: Free energies of the 3×3 CDW mode in 1H-TaS$_2$ from DFT (blue crosses) and downfolded models. (a) Interacting model with partially screened quantities from constrained theories cRPA and cDFPT (start from cDFPT parabola). (b) Interacting model with partially screened quantities from unscreening (start from DFPT parabola). (c) Non-interacting model with fully screened quantities (start from DFPT parabola).
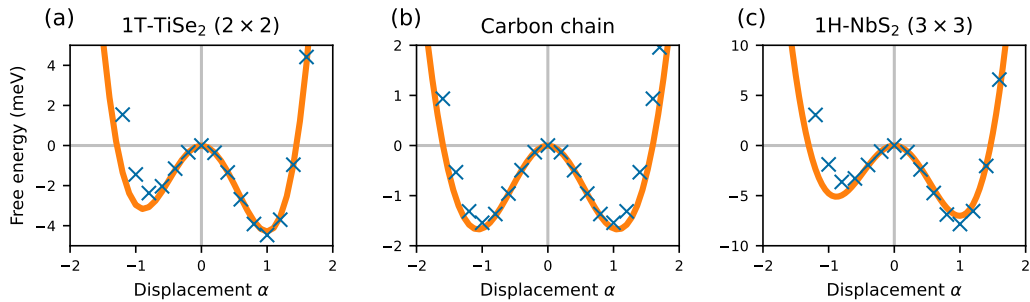
Figure 4: Free energies of (a) the 2×2 CDW in 1T-TiSe$_2$, (b) the CDW in the carbon chain, and (c) the 3×3 CDW in 1H-NbS$_2$. The blue crosses are data points from DFT and the orange curves are the model III results.

3.1 Influence of Wannier orbitals and electronic Hilbert space dimension

Since the electronic Hamiltonian [Eq. (3)] is represented via Wannier functions, we have a certain freedom of choice. From a computational standpoint, we are aiming for a maximal reduction of the dimension of the single-particle Hilbert space, while maintaining a reasonable level of accuracy. Thus, the natural question arises: How many and which Wannier orbitals to choose to create the single-particle Hilbert space?

For 1H-TaS$_2$, we compare a "minimal" and a "maximal" model involving, respectively, three and eleven Wannier orbitals per unit cell: In the case of three orbitals, there are three d-type orbitals on the Ta atom ($d_{z^2}, d_{x^2-y^2}, d_{xy}$), and in the case of eleven orbitals, there are five d-type orbitals on the Ta atom ($d_{z^2}, d_{xz}, d_{yz}, d_{x^2-y^2}, d_{xy}$) and three p-type orbitals on both S atoms (p_x, p_y, p_z). Note that these are the Hilbert space dimensions on the primitive unit cell. On the 3×3 supercell calculations, the dimensions are 27 and 99 respectively.

We compare the energy-displacement curves resulting from model III for both Hilbert space sizes to DFT in Fig. 5. While the results are similar in both cases, the eleven orbital model is slightly closer to full DFT than the three orbital model. In the eleven-orbital model, the displacement potentials directly induce changes in the d-p hybridization. We speculate that anharmonicities associated with these rehybridization terms are responsible for the slightly improved accuracy of the eleven band model.
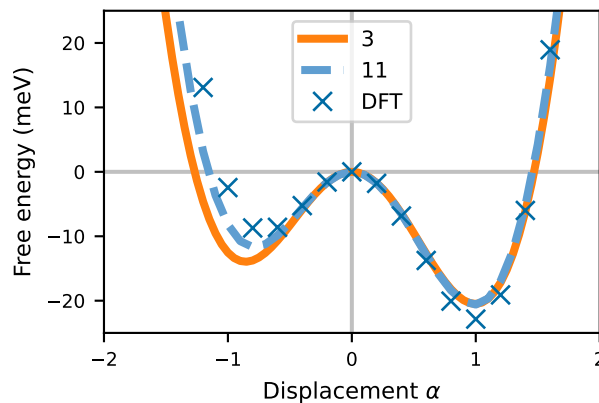
Figure 5: Free energies of the 3×3 CDW in 1H-TaS$_2$. We show DFT data points (blue crosses), model III results for three Wannier orbitals (orange solid curve), and model III results for eleven Wannier orbitals (blue dashed curve).

3.2 Electronically generated anharmonicities

Models I, II, and III are based on the electronic structure at the symmetric equilibrium positions of the atoms, as well as the linear response to displacements that is accessible in DFPT. By construction, models II and III guarantee agreement with the full DFT calculation at small displacements u, up to order u^2 in the energy and up to order u in the electronic structure. One might wonder if these models, based on linear response, can ever be useful for the description of the distorted phase, which is necessarily stabilized by anharmonicity and terms of order u^3, u^4, and beyond.

The close match between the significantly anharmonic DFT potential energy landscapes and models II and III in Figs. 3, 4, and 5 at $|\alpha| > 1$ might thus come as a surprise. The reason behind the good match even in the anharmonically dominated region can be understood in the following sense: Linear changes in the electronic potential lead to non-linear changes in eigenvalues of the electronic Hamiltonian and therefore in the total energy. Thus, if the low-energy electrons are responsible for the anharmonicity that stabilizes the CDW, then a low-energy electronic model based on DFPT quantities has the possibility to describe this.

The emergence of electronically driven anharmonicities can be illustrated with an electronic two-level system, $H_{\text{el}}^0 = \Delta \sigma_z$, coupled linearly to a nuclear displacement u through $H_{\text{el-n}} = u \cdot d \sigma_x$ [following Eq. (9)]. Here, σ_i denote Pauli matrices, 2Δ is the level-splitting and d encodes the strength of the coupling of electrons to nuclear displacements as in Eq. (9). The ground state eigenvalue of $H_{\text{el}}^0 + H_{\text{el-n}}$ reads $E_0 = -\sqrt{\Delta^2 + (du)^2} \approx -\Delta \left(1 + \frac{1}{2}\left(\frac{du}{\Delta}\right)^2 - \frac{1}{8}\left(\frac{du}{\Delta}\right)^4 + \dots\right)$. Thus, electronically generated anharmonicities appear at displacements on the order $u \approx \Delta/d$. Taking the level splitting Δ as a proxy for the electronic bandwidth $W \sim \Delta$ or for the inverse of the density of states at the Fermi level $\rho \sim 1/\Delta$, we have electronically generated anharmonicities appearing at displacements on the order $u \approx W/d \approx 1/(\rho d)$. In other words, systems with strong electron-lattice coupling and high density of states at the Fermi level are expected to be domains where the linearized electron-lattice coupling preferably works. In addition, the approximation of a linearized electron-lattice coupling as in Eq. (9) has also been successfully applied to describe polaronic lattice distortions [80, 81].

This hypothesis is further corroborated by the comparison of energy-displacement curves for 1H-TaS$_2$ at different electronic smearings to those of the related system 1H-WS$_2$, in Fig. 6.

The electronic band structure of WS$_2$ [82] is very similar to the one of TaS$_2$ (see Fig. 2b) with the key difference that it has one additional valence electron per unit cell. Hence, the half-

(a)   (b)
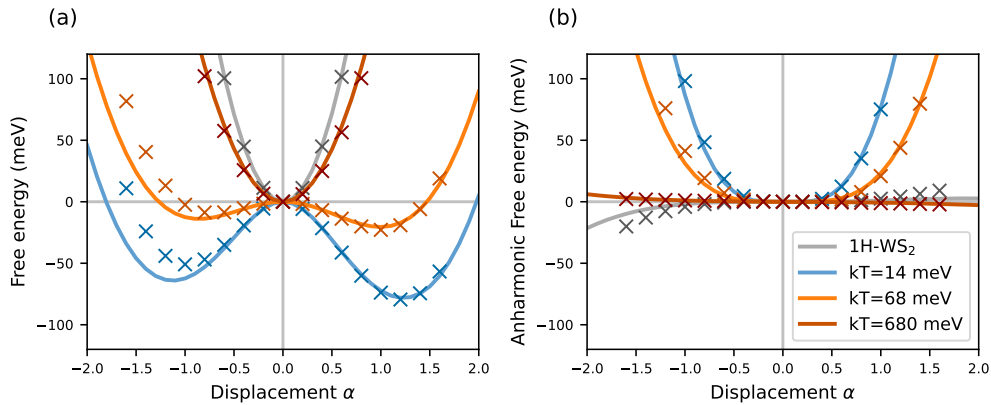
Figure 6: (a) Free energy and (b) anharmonic part of the free energy for 1H-TaS$_2$ at electronic smearings $kT = 14$ meV (blue), 68 meV (orange), 680 meV (dark red) and for 1H-WS$_2$ at smearing $kT = 68$ meV. Solid lines originate from model III and crosses from DFT. Even though the inputs for model III (see Table 1) were generated at the electronic temperature $T_{\mathrm{DFT}} = 68$ meV, we can still evaluate the free energy at higher or lower model temperatures T_{M} and get a good agreement with DFT.

filled conduction band of TaS$_2$ becomes completely filled in the WS$_2$ case, which renders WS$_2$ semiconducting and quenches the response of the low energy electronic system. Similarly, an increased electronic smearing/temperature quenches the response of the low-energy electronic system. Both WS$_2$ and TaS$_2$ at high smearing, are dynamically stable, which is indicated by the positive second order of the free energy in Fig. 6a. This tells us that at least the harmonic term is significantly affected by the occupation of the low-energy subspace. Furthermore, in Fig. 6b, we show the corresponding anharmonic part of the free energies. The flat shape of the high smearing (dark red) and the WS$_2$ (gray) curves show that the anharmonicity is strongly reduced compared to the low smearing cases. These observations suggest that the anharmonicities associated with the CDW formation in 1H-TaS$_2$ indeed originate to a large extent from non-linearities in the response of the low-energy electronic system to the external displacement-induced potentials.

Anharmonicities associated with the non-linear low-energy electronic response comprise single-particle and Coulomb contributions. We analyze these contributions diagrammatically in the following for the grand canonical potential Ω:

Model III has the Coulomb contributions accounted for indirectly via the fully screened DFPT deformation-induced potential and the diagrams contributing to anharmonicities in Ω are of the following types:

$$\Omega^{\mathrm{III}}_{\mathrm{anh}} = \;\; + \;\; + \ldots \tag{17}$$

Model II has explicit Coulomb interaction entering and the diagrammatic content is determined by the approximation used to treat the Coulomb interaction in model II. When solving model II in self-consistent Hartree approximation, we generate terms screening the deformation-induced potential according to Eq. (14). Thus, the anharmonic contributions to the grand potential in model II, $\Omega^{\mathrm{II}}_{\mathrm{anh}}$, contain those diagrams also present in model III but also further ones. For example, at order u^4, model II contains a diagram of the form

$$\tag{18}$$

which is not present in model III.

Both the Green's function (not shown here) and total energy or grand canonical potential in models II and III agree at small displacements (by construction) and disagree at higher orders in u, and their difference scales with the strength of the Coulomb interaction. Fundamentally, the Green's function of the exact DFT solution contains interaction-mediated anharmonic response to displacements, just like model II does. At the same time, in our current implementation model II only contains Hartree-like diagrams of this kind and lacks other diagram topologies present in the exact DFT solution. These additional diagrams can lead to substantial error cancellation. Thus, it is hard to make general arguments about which model to prefer beyond order u^2, given the opaqueness of the underlying DFT exchange-correlation functional. We speculate that cancellations similar to those occurring in second order [73, 76] in u could be also effective in higher orders. In our numerical studies, we find that the total energy curves of model II and III are relatively close for the systems studied here.

4 Downfolding-based molecular dynamics

So far we have seen that the downfolded models can reproduce total free energies from DFT. In the following Section 4.1, we assess the computational speed of these models, which ultimately paves the way to enhanced sampling simulations based on MD. As a demonstration of this enhancement, we perform the downfolding-based MD for the example case of monolayer 1H-TaS$_2$ in Section 4.2.

4.1 Benchmark of model III against DFT: Force and free energy calculations

To demonstrate the performance gain of model III, we benchmark the calculation of forces and free energies against DFT. For this benchmark, we perform structural relaxations of 1H-TaS$_2$ starting from random displacements $|u_i| < 0.01$ Bohr—to mimic the conditions of a MD simulation step—on different supercells. Durations are averaged over five steps, excluding the first step starting from the initial guess for the density in the DFT case. Calculations are performed on identical machines, using equivalent computational parameters (cf. Appendix C). The results are shown in Fig. 7.

More precisely, we benchmark two implementations of model III: Calculations on finite k meshes, as shown in the previous Section 3, currently require a lot of memory to store the deformation-induced potential in the real-space ($d_{R,R'}$) and reciprocal-space ($d_{q=0,k}$) representations, which limits the system to similar sizes as achievable in DFT (Fig. 7a). Thus, in this section, we instead use a sparse representation, which uses significantly less memory (Fig. 7b), reaching linear scaling with the system size (cf. Ref. [46]), but is currently restricted to $k = 0$, appropriate for large supercells. It also increases the time needed to initialize the program (Fig. 7c, d), which however does not influence the MD simulations. Comparing to the same DFT program we use to obtain the parameters for the downfolded model, i.e., the plane-wave code QUANTUM ESPRESSO [83, 84], we find a speedup of about five orders of magnitude in the downfolding approach for the relevant systems (Fig. 7e, f). Note that our implementation is based on NUMPY and SCIPY [85, 86] and that optimizations both on the *ab initio* and on the model side are possible.

The computational advantage from the non-interacting model III over DFT is easily explained: While DFT relies on the self-consistent solution of the Kohn-Sham system, model III only needs a single matrix diagonalization to solve the Schrödinger equation, thus making it the fastest of all three models. Model I and II on the other hand, incorporate the Coulomb interaction through a self-consistent Hartree algorithm. Assuming a typical number of ~ 10 cycles needed for convergence the speedup should be on the order of 10^4 rather than 10^5. Most importantly, through downfolding, the matrix of all downfolded models only covers the
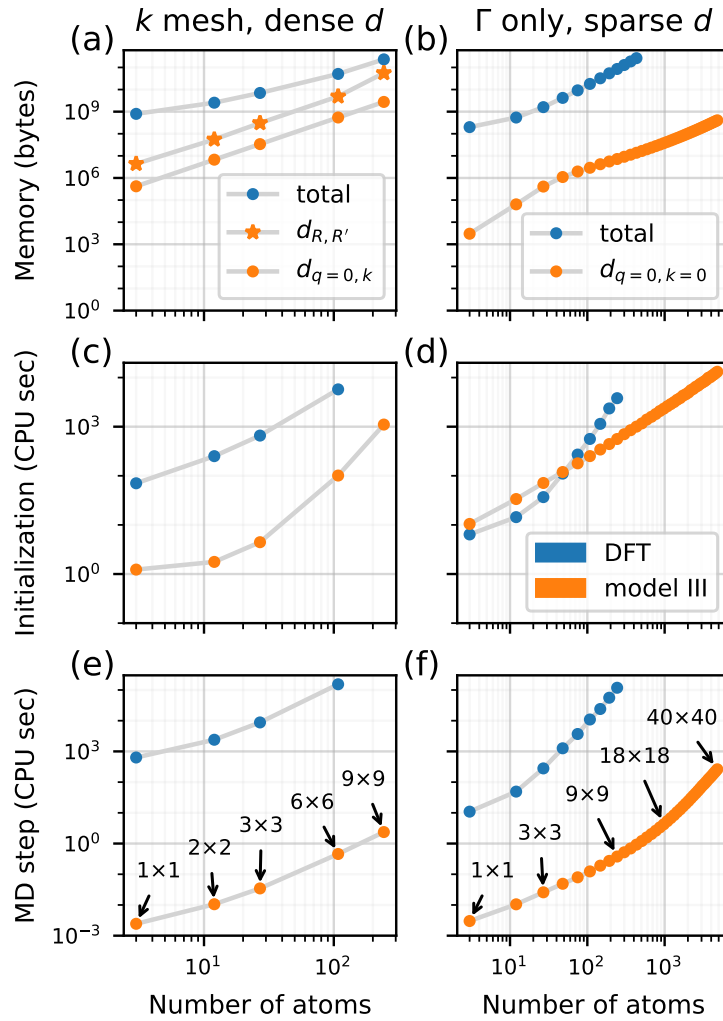
Figure 7: Comparison of (a, b) memory requirements, (c, d) initialization times, and (e, f) durations of energy and forces calculations using QUANTUM ESPRESSO (blue) and our PYTHON implementations of model III (orange) (cf. Appendix C). We consider (a, c, e) k meshes of constant density and (b, d, f) the Γ-only case, for which model III has been implemented using arrays of sparse matrices for the electron-phonon coupling $d_{i\alpha\beta}$. The DFT calculations have been parallelized over plane waves and real-space grids (-nk 1 -nd 1) using 40 CPUs; the model calculations have been run serially. In both cases, Intel Skylake 6148 processors have been used.

low-energy subspace of the electronic structure, as opposed to DFT, whose matrix accounts for low- and high-energy bands.

In fact, most of the time is spent on setting up the Hamiltonian matrix and evaluating the forces [Eq. (11)]. To guarantee that the former is Hermitian and to make the use of sparse matrices more efficient, we have symmetrized $d_{R,R'\alpha\beta} = d^*_{R-R',-R'\beta\alpha}$ and neglected matrix elements smaller than 1 % of the maximum, the effect of which on the free-energy landscape is negligible.

4.2 Enhanced sampling simulations based on downfolded model III

We now perform enhanced sampling simulations based on MD with the downfolding scheme defined by model III. To this end, we implemented a PYTHON-based tight-binding solver [74],
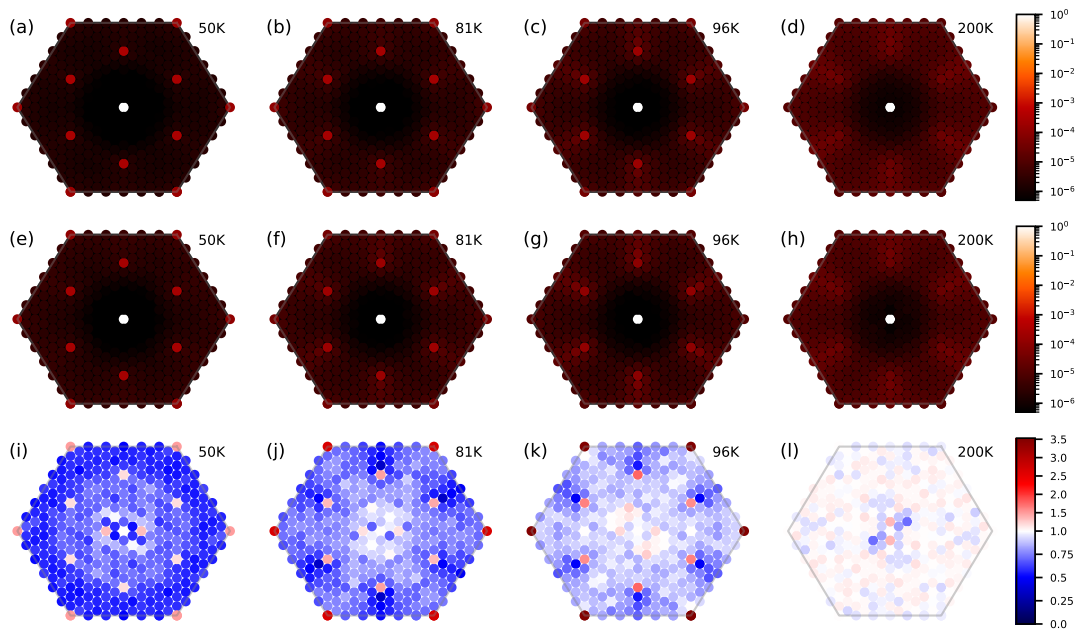
Figure 8: Structure factors $\langle S(\boldsymbol{q})\rangle_T$ [Eq. 19] for 1H-TaS$_2$ on the 18 × 18 supercell. (a–d) Structure factor S_{CL} from classical MD. (e–h) Structure factor S_{PI} from PIMD. The peaks at $\boldsymbol{q} = 2/3\,\Gamma\mathrm{M}$ and $\boldsymbol{q} = \mathrm{K}$ for $T = 50$ K are characteristic for the 3 × 3 CDW. At higher temperatures, the peaks are broadened and reduced in intensity. (i–l) Ratio of structure factors $S_{\mathrm{CL}}/S_{\mathrm{PI}}$ from classical and path integral MD. A value close to 1 (indicated in white) corresponds to minimal differences between classical and quantum simulations.

which delivers displacement field dependent forces and total free energies to the i-PI (path integral) MD engine [87].

As stated in the previous section, we find a speedup of about five orders of magnitude in the downfolding approach. Thus, the downfolding approaches make larger system sizes and longer time scales well accessible. While for instance Ref. [88] simulates the dynamics of 3 × 3 supercells of 1H-NbS$_2$ with *ab initio* MD (AIMD) for time scales of about 6 to 12 ps, the downfolding-based MD allows us to address much larger 18 × 18 supercells for time scales of about 500 ps using a similar amount of CPU hours.[1]

For monolayer 1H-TaS$_2$, we performed classical (and path integral) replica exchange MD simulations (see Appendix D) on the 18 × 18 supercells using 26 replicas (and 10 beads) spanning a temperature range from 50 to 200 K in the canonical (NVT) ensemble. In each MD step ν we record the position vectors of all nuclei $\boldsymbol{R}_l(\nu, T)$ for all temperatures T. Defining the static structure factor

$$S(\boldsymbol{q}) = \frac{1}{N_{\mathrm{at}}^2} \left| \sum_{l=1}^{N_{\mathrm{at}}} e^{-i\boldsymbol{q}\cdot\boldsymbol{R}_l} \right|^2 \qquad (19)$$

for a given atomic configuration $\boldsymbol{R}_l$, we obtain the temperature-dependent MD ensemble averaged structure factors $\langle S(\boldsymbol{q})\rangle_T$. We confine the summation to the positions of the tantalum atoms and normalize the structure factor such that $S(\boldsymbol{q} = 0) = 1$. The static structure factor is the frequency integrated version of the dynamic structure factor $S(\boldsymbol{q}) = \hbar \int_{-\infty}^{+\infty} S(\boldsymbol{q}, \omega)d\omega$. Furthermore, it contains both Bragg and all orders of thermal diffuse scattering contributions.

---

[1]The actual simulated times are 430 ps and 930 ps for the path integral (classical) replica exchange MD.
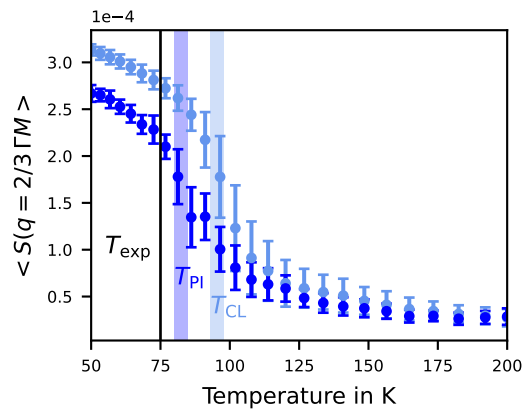
Figure 9: Structure factor $\langle S(\boldsymbol{q} = 2/3\,\Gamma M)\rangle_T$ at the characteristic CDW wavevector $\boldsymbol{q} = 2/3\,\Gamma M$ for the classical MD (light blue) and path integral MD (blue). The effective shift of the PIMD curve toward the experimental value can be attributed to nuclear quantum effects.

The resultant structure factor maps on the first Brillouin zone of 1H-TaS$_2$ are shown in Fig. 8 for temperatures $T = 50, 81, 96, 200$ K.[2] The upper row corresponds to classical MD simulations. At 50 K, we find peaks in the structure factor at $\boldsymbol{q} = 2/3\,\Gamma M$, which are characteristic of the 3×3 CDW. These peaks broaden and become reduced in intensity upon increasing temperature. Fig. 9 shows the temperature dependence of $\langle S(\boldsymbol{q} = 2/3\,\Gamma M)\rangle_T$ in more detail. We see the aforementioned temperature-induced reduction in $\langle S(\boldsymbol{q} = 2/3\,\Gamma M)\rangle_T$ with an inflection point around $T_{CL} \approx 96$ K. We take this inflection point as the finite system size approximation to the phase transition temperature that would be expected for an infinitely large simulation cell.

While a 3×3 CDW has been observed in monolayer 1H-TaS$_2$ [89], the exact transition temperature is not known in this system. For the three-dimensional bulk of 2H-TaS$_2$, CDW transition temperatures on the order of $T_{exp} \approx 75$ K have been reported [90–95]. Our classical finite system size estimate exceeds these temperatures by about 25 %. One possible origin of this deviation can be quantum fluctuations in nuclear degrees of freedom.

Therefore, we performed path integral MD (PIMD) replica exchange simulations to assess the influence of nuclear quantum effects on the CDW formation. The PIMD structure factor maps in the middle row of Fig. 8 behave qualitatively similar to the classical counterpart. Their ratio is quantitatively illustrated in the lowest row. The overall area of the Brillouin zone turns from blue to white by heating up the system. Thus, as expected, the classical and quantum simulations agree at high temperatures. However, the CDW fingerprints ($\boldsymbol{q} = 2/3\,\Gamma M$ and $\boldsymbol{q} = K$) clearly increase in intensity and survive at higher temperatures in the classical case. Note that while there is no phonon instability at $\boldsymbol{q} = K$, the corresponding displacements are commensurate with a 3×3 superstructure and couple anharmonically to the soft modes at $\boldsymbol{q} = 2/3\,\Gamma M$. This explains the high ratios at the Brillouin-zone corners in Fig. 8 (i–k), especially in the vicinity of the transition temperature.

This difference between classical and quantum simulations can be inspected in more detail in Fig. 9. While the qualitative shape of the PIMD curve (dark blue) is similar to the classical MD (light blue) simulation, we find an effective shift of the curve and an inflection point at $T_{PI} \approx 82$ K. Thus, quantum effects can significantly reduce the estimated CDW transition temperature as compared to the classical estimate and lead to a closer match with experiment.

---

[2]We show those $\boldsymbol{q}$ vectors compatible with the periodic boundary conditions on the 18×18 unit cell.

From these demonstrator calculations it becomes clear that the downfolding-based MD developed in this work opens the gate for precise computational studies of CDW (thermo)dynamics, which were inaccessible in the domain of *ab initio* MD hitherto.

5 Conclusions

We presented three downfolding schemes to describe low-energy physics of electron-lattice coupled systems—in particular CDWs—on a similar level of accuracy as full *ab initio* DFT: Model I is based on constrained theories and models II and III are based on unscreening, where model II features explicit Coulomb interactions and model III is effectively non-interacting. The central goal of these downfolding schemes is to reduce the complexity of first-principles electronic structure calculations. This is achieved by mapping the general solid-state Hamiltonian onto minimal quantum lattice models with only a few localized Wannier orbitals per unit cell. The solution of these models is significantly faster than DFT. For model III, we found a speedup of about five orders for the example case of monolayer 1H-TaS$_2$. Despite this enormous speedup and complexity reduction, we demonstrated a quantitative recovery of DFT potential energy surfaces in downfolded models II and III.

As a demonstration, we performed classical and path integral MD simulations using model III of the 1H-TaS$_2$ CDW systems. The downfolding-based speedup opens the gate for enhanced sampling techniques and path integral simulations of nuclear quantum effects on the CDW transition. This makes downfolded models the method of choice for precise computational studies of dynamics and thermodynamics in CDW systems, which were hitherto largely inaccessible to *ab initio* MD.

While we focussed, here, on Born-Oppenheimer MD, the Hamiltonians resulting from downfolded models I–III are generic and likely applicable also when dealing with non-adiabatic phenomena, electron-lattice coupled dynamics in excited electronic states, and situations where strong electron-electron correlations are at play. Due to the explicit account of Coulomb interactions in models I and II, these schemes offer themselves for treatments of situations where electronic interaction effects beyond semilocal DFT are to be included in studies of coupled electron-nuclear dynamics. Furthermore, anharmonic force constants and non-perturbative electron-phonon couplings [96] can be incorporated into the downfolded models to expand the accuracy to even larger lattice distortions.

Future applications of the downfolding schemes developed here might reach to the physics of (nonequilibrium) phase transitions involving CDW order [10–18] or the interplay of correlations and (dis)ordering [19,97] as well as driven quantum systems [4–6]. Beyond potential energy surfaces, the downfolded models can also be used to study the effective electronic structure in the presence of atomic dynamics.

Acknowledgments

Data availability   The source code and data associated with this work are available on Zenodo [98].

A   Free energy calculations of the downfolded models in Hartree approximation

The Coulomb interaction in models I and II renders the electronic Hamiltonian interacting and requires approximate treatments. Here, we solve the interacting Hamiltonian in Hartree approximation, which is the simplest mean-field approximation and as such requires a self-consistency loop.

For the Coulomb interaction, we assume here a density-density type interaction

$$H_{\text{el}}^1 = \frac{1}{2N} \sum_{\boldsymbol{q} \boldsymbol{k} \boldsymbol{k}' \alpha \beta} U_{\alpha\beta}^{\boldsymbol{q}} c_{\boldsymbol{k}+\boldsymbol{q}\alpha}^{\dagger} c_{\boldsymbol{k}'\beta}^{\dagger} c_{\boldsymbol{k}'+\boldsymbol{q}\beta} c_{\boldsymbol{k}\alpha}, \tag{A.1}$$

with $U_{\alpha\beta}^{\boldsymbol{q}}$ being cRPA density-density matrix elements evaluated at momentum transfer $\boldsymbol{q}$.

The Hartree decoupling of Eq. (A.1) reads

$$H_{\text{el}}^1 = \frac{1}{N} \sum_{\boldsymbol{k} \boldsymbol{k}' \alpha \beta} U_{\alpha\beta}^{\boldsymbol{q}=0} \left(c_{\boldsymbol{k}\alpha}^{\dagger} c_{\boldsymbol{k}\alpha} \left\langle c_{\boldsymbol{k}'\beta}^{\dagger} c_{\boldsymbol{k}'\beta} \right\rangle - \frac{1}{2} \left\langle c_{\boldsymbol{k}\alpha}^{\dagger} c_{\boldsymbol{k}\alpha} \right\rangle \left\langle c_{\boldsymbol{k}'\beta}^{\dagger} c_{\boldsymbol{k}'\beta} \right\rangle \right). \tag{A.2}$$

Since the DFT input parameters of models I and II already contain Coulomb contributions, we have to avoid double counting. The hopping terms $t_{\boldsymbol{k}\alpha\beta}^0$ stem from the Kohn-Sham eigenvalues of the undistorted structure, which contain (among others) a Hartree term. Here, we choose H_{DC} to compensate for the Hartree term of the undistorted structure:

$$H_{\text{DC}} = -\frac{1}{N} \sum_{\boldsymbol{k} \boldsymbol{k}' \alpha \beta} U_{\alpha\beta}^{\boldsymbol{q}=0} \left(c_{\boldsymbol{k}\alpha}^{\dagger} c_{\boldsymbol{k}\alpha} \left\langle c_{\boldsymbol{k}'\beta}^{\dagger} c_{\boldsymbol{k}'\beta} \right\rangle_0 - \frac{1}{2} \left\langle c_{\boldsymbol{k}\alpha}^{\dagger} c_{\boldsymbol{k}\alpha} \right\rangle_0 \left\langle c_{\boldsymbol{k}'\beta}^{\dagger} c_{\boldsymbol{k}'\beta} \right\rangle_0 \right), \tag{A.3}$$

where $\langle \ldots \rangle_0$ denotes expectation values obtained for the undistorted structure.

We introduce the Hartree potentials $\overline{U}_\alpha$ and $\overline{U}_\alpha^0$ for the distorted and undistorted structures, respectively,

$$\overline{U}_\alpha = \sum_\beta U_{\alpha\beta}^{\boldsymbol{q}=0} n_\beta \quad \text{and} \quad \overline{U}_\alpha^0 = \sum_\beta U_{\alpha\beta}^{\boldsymbol{q}=0} n_\beta^0, \tag{A.4}$$

where $n_\beta^{(0)} = \frac{1}{N} \sum_{\boldsymbol{k}'\beta} \langle c_{\boldsymbol{k}'\beta}^{\dagger} c_{\boldsymbol{k}'\beta} \rangle_{(0)}$ denotes local orbital occupations. Then, the electronic mean-field Hamiltonian written in the Wannier orbital basis of the supercell reads

$$H_{\text{el}} + H_{\text{el-n}} = \sum_{\boldsymbol{k}\alpha\beta} \left(t_{\boldsymbol{k}\alpha\beta}^0 + \boldsymbol{u} \boldsymbol{d}_{\boldsymbol{k}\alpha\beta} + (\overline{U}_\alpha - \overline{U}_\alpha^0)\delta_{\alpha\beta} \right) c_{\boldsymbol{k}\alpha}^{\dagger} c_{\boldsymbol{k}\beta} - \frac{1}{2} \sum_{\alpha\beta} U_{\alpha\beta}^{\boldsymbol{q}=0} (n_\alpha n_\beta - n_\alpha^0 n_\beta^0). \tag{A.5}$$

This Hamiltonian is solved self-consistently. The converged electronic dispersion ε_{kn} and occupations n_α are used to determine the free energy:

$$F_{\text{el}} = \frac{2}{N} k_B T \sum_{n\boldsymbol{k}} \ln\Big(f\big[-(\varepsilon_{\boldsymbol{k}n} - \mu)/kT\big]\Big) + \mu N_{\text{el}} - \frac{1}{2}\sum_{\alpha\beta} U_{\alpha\beta}^{\boldsymbol{q}=0}(n_\alpha n_\beta - n_\alpha^0 n_\beta^0). \tag{A.6}$$

The Coulomb matrix $U_{\alpha\beta}^{\boldsymbol{q}}$ contains one divergent eigenvalue for $\boldsymbol{q} \to 0$, which is associated with the homogeneous charging of the system. Since we are working at fixed system charge, we exclude the divergent contribution of $U_{\alpha\beta}^{\boldsymbol{q}}$. In practice we perform the eigenvector decomposition of Eq. (15) from Ref. [99] and exclude the contribution from the leading eigenvector.

B Perturbation expansion of grand potential and free energy

Changes of the grand potential of non-interacting electrons due to atomic displacements can be straightforwardly evaluated using diagrammatic perturbation theory [100]:

$$\Omega = \Omega\big|_0 + \sum_i \Omega_i^{(1)}\big|_0 u_i + \frac{1}{2}\sum_{ij}\Omega_{ij}^{(2)}\big|_0 u_i u_j + \dots \tag{B.1}$$

$$\equiv \Omega\big|_0 + \quad + \quad + \dots \tag{B.2}$$

Without loss of generality, we consider $\boldsymbol{q} = 0$ in Eq. (9) and drop the corresponding subscript.

In first order, we then have

$$\boldsymbol{\Omega}^{(1)} = \frac{kT}{N}\sum_{\boldsymbol{k}n\nu}\boldsymbol{d}_{\boldsymbol{k}nn}\frac{1}{\mathrm{i}\omega_\nu - \varepsilon_{\boldsymbol{k}n} + \mu} = \frac{1}{N}\sum_{\boldsymbol{k}n}\boldsymbol{d}_{\boldsymbol{k}nn}f(\varepsilon_{\boldsymbol{k}n} - \mu), \tag{B.3}$$

with the Matsubara frequency $\omega_\nu = (2\nu + 1)\pi kT$.

In second order, we have

$$\Omega^{(2)} = \frac{kT}{N}\sum_{\boldsymbol{k}mn\nu}\boldsymbol{d}_{\boldsymbol{k}mn}\frac{1}{\mathrm{i}\omega_\nu - \varepsilon_{\boldsymbol{k}m} + \mu}\frac{1}{\mathrm{i}\omega_\nu - \varepsilon_{\boldsymbol{k}n} + \mu}\boldsymbol{d}_{\boldsymbol{k}nm}^T \tag{B.4}$$

$$= \frac{1}{N}\sum_{\boldsymbol{k}mn}\boldsymbol{d}_{\boldsymbol{k}mn}\frac{f(\varepsilon_{\boldsymbol{k}m} - \mu) - f(\varepsilon_{\boldsymbol{k}n} - \mu)}{\varepsilon_{\boldsymbol{k}m} - \varepsilon_{\boldsymbol{k}n}}\boldsymbol{d}_{\boldsymbol{k}nm}^T. \tag{B.5}$$

We deliberately have omitted the superscript zero from $\varepsilon_{\boldsymbol{k}n}$ [cf. Eq. (3)] as in our models with linear electron-phonon coupling these formulas also hold for $\boldsymbol{u} \neq 0$ as long as $\boldsymbol{d}$ is represented in the electronic eigenbasis.

The number of electrons N_{el} is typically conserved in DFT and MD calculations, so we are instead interested in the canonical ensemble and the free energy

$$F(N_{\text{el}}) = \Omega(\mu(N_{\text{el}})) + \mu(N_{\text{el}})N_{\text{el}}. \tag{B.6}$$

Its first derivative with respect to displacements is

$$F_i^{(1)} = \frac{\mathrm{d}F}{\mathrm{d}u_i} = \frac{\partial\Omega}{\partial u_i} + \left[\frac{\partial\Omega}{\partial\mu} + N_{\text{el}}\right]\frac{\mathrm{d}\mu}{\mathrm{d}u_i} = \Omega_i^{(1)}, \tag{B.7}$$

since $\partial\Omega/\partial\mu = -N_{\text{el}}$. In other words, the expression for the forces [cf. Eq. (11)] is the same in the canonical and the grand-canonical ensemble.

For the unscreening of the force constants (cf. Section 2.1), we also need access to the second derivative of the free energy at constant electron density,

$$F_{ij}^{(2)} = \frac{\mathrm{d}F_i^{(1)}}{\mathrm{d}u_j} = \frac{\partial \Omega_i^{(1)}}{\partial u_j} + \frac{\partial \Omega_i^{(1)}}{\partial \mu} \frac{\mathrm{d}\mu}{\mathrm{d}u_j}.$$ (B.8)

Expectedly, the first term on the right is $\Omega_{ij}^{(2)}$ from Eq. (B.5). Here, the second term does not vanish, at least not for monochromatic perturbations with $\boldsymbol{q} = 0$ [101]. The change of the chemical potential upon atomic displacements follows from the electron conservation,

$$0 \overset{!}{=} \frac{\mathrm{d}N_{\mathrm{el}}}{\mathrm{d}\boldsymbol{u}} = \frac{1}{N} \frac{\mathrm{d}}{\mathrm{d}\boldsymbol{u}} \sum_{\boldsymbol{k}n} f(\varepsilon_{\boldsymbol{k}n} - \mu) = -\frac{1}{N} \sum_{\boldsymbol{k}n} \Big[\boldsymbol{d}_{\boldsymbol{k}nn} - \frac{\mathrm{d}\mu}{\mathrm{d}\boldsymbol{u}} \Big] \delta(\varepsilon_{\boldsymbol{k}n} - \mu),$$ (B.9)

with $\delta(\varepsilon) = -\mathrm{d}f(\varepsilon)/\mathrm{d}\varepsilon$. We have used the Hellmann-Feynman theorem,

$$\frac{\mathrm{d}\varepsilon_{\boldsymbol{k}n}}{\mathrm{d}\boldsymbol{u}} = \frac{\mathrm{d}}{\mathrm{d}\boldsymbol{u}} \langle \boldsymbol{k}n | H_{\mathrm{el}}^0 + H_{\mathrm{el\text{-}n}} | \boldsymbol{k}n \rangle = \langle \boldsymbol{k}n | \frac{\mathrm{d}}{\mathrm{d}\boldsymbol{u}} (H_{\mathrm{el}}^0 + H_{\mathrm{el\text{-}n}}) | \boldsymbol{k}n \rangle \equiv \boldsymbol{d}_{\boldsymbol{k}nn}.$$ (B.10)

Note that here the matrix element of the deformation-induced potential $\boldsymbol{d}_{\boldsymbol{k}nn}$ is represented in the basis of eigenstates $|\boldsymbol{k}n\rangle$ of the *perturbed* Hamiltonian. Rearranging Eq. (B.9) shows that the change of the chemical potential is nothing but the Fermi surface (FS) average of the intraband deformation-induced potential,

$$\frac{\mathrm{d}\mu}{\mathrm{d}\boldsymbol{u}} = \frac{\sum_{\boldsymbol{k}n} \boldsymbol{d}_{\boldsymbol{k}nn} \delta(\varepsilon_{\boldsymbol{k}n} - \mu)}{\sum_{\boldsymbol{k}n} \delta(\varepsilon_{\boldsymbol{k}n} - \mu)} \equiv \langle \boldsymbol{d}_{\boldsymbol{k}nn} \rangle_{\mathrm{FS}}.$$ (B.11)

From Eq. (B.3), we can also readily evaluate

$$\frac{\partial \boldsymbol{\Omega}^{(1)}}{\partial \mu} = \frac{1}{N} \sum_{\boldsymbol{k}n} \boldsymbol{d}_{\boldsymbol{k}nn} \delta(\varepsilon_{\boldsymbol{k}n} - \mu) \equiv \rho(\mu) \langle \boldsymbol{d}_{\boldsymbol{k}nn} \rangle_{\mathrm{FS}},$$ (B.12)

where ρ is the electronic density of states per unit cell. Inserting Eqs. (B.11) and (B.12) into Eq. (B.8) yields

$$\Delta C_{ij}^{\mathrm{III}} = \Omega_{ij}^{(2)} + \rho(\mu) \langle d_{i\boldsymbol{k}nn} \rangle_{\mathrm{FS}} \langle d_{j\boldsymbol{k}nn} \rangle_{\mathrm{FS}}.$$ (B.13)

The first term are the force constants in the grand canonical ensemble, i.e., at constant chemical potential. The second term is the correction for going from the grand canonical to the canonical ensemble.

C Computational parameters for DFT

All DFT and DFPT calculations are carried out using QUANTUM ESPRESSO [83,84]. The modification that is required for cDFPT is described in detail in Ref. [64]. For the transformation of the electronic energies and electron-phonon couplings to the Wannier basis, we use WANNIER90 [102] and the EPW code [103–105]. The cRPA Coulomb interaction was calculated using RESPACK [106]. In the following, we will list the specific DFT and DFPT parameters for each material individually:

1H-TaS$_2$ Hartwigsen-Goedecker-Hutter (HGH) pseudopotentials [107, 108]; $18 \times 18 \times 1$ $\boldsymbol{k}$ mesh and $6 \times 6 \times 1$ $\boldsymbol{q}$ mesh for unit cell; Fermi-Dirac smearing of 5 mRy (Gaussian smearing of 0.1 Ry for Fig. 7b, d, f); energy convergence threshold of 10^{-15} Ry (10^{-8} Ry per unit cell for Fig. 7); lattice constant of 3.39 Å. The cRPA Coulomb interaction has been calculated on a $32 \times 32 \times 1$ $\boldsymbol{q}$ mesh taking 80 electronic bands into account.

1H-NbS$_2$ HGH pseudopotentials [107,108]; $18 \times 18 \times 1$ $\boldsymbol{k}$ mesh and $6 \times 6 \times 1$ $\boldsymbol{q}$ mesh for unit cell; Fermi-Dirac smearing of 3 mRy; lattice constant of 3.34 Å.

1H-WS$_2$ HGH pseudopotentials [107,108]; $18 \times 18 \times 1$ $\boldsymbol{k}$ mesh and $6 \times 6 \times 1$ $\boldsymbol{q}$ mesh for unit cell; Fermi-Dirac smearing of 5 mRy; lattice constant of 3.23 Å.

1T-TiSe$_2$ Ultrasoft pseudopotential [109] from the SSSP library [110,111]; $18 \times 18 \times 1$ $\boldsymbol{k}$ mesh and $6 \times 6 \times 1$ $\boldsymbol{q}$ mesh for unit cell; Fermi-Dirac smearing of 5 mRy; lattice constant of 3.54 Å.

Carbon chain Optimized norm-conserving Vanderbilt pseudopotential (ONCVPSP) [112] from the PSEUDODOJO library [113]; $200 \times 1 \times 1$ $\boldsymbol{k}$ mesh and $20 \times 1 \times 1$ $\boldsymbol{q}$ mesh for unit cell; Fermi-Dirac smearing of 5 mRy; lattice constant of 1.30 Å.

In all cases, we have applied the Perdew-Burke-Ernzerhof (PBE) functional [114], set the plane-wave cutoff to 100 Ry, and minimized forces and pressure in the periodic directions to below 1 μRy/Bohr and 0.1 kbar. We have used a unit-cell dimension of 15 Å to separate images in the non-periodic directions.

D Replica exchange

In order to characterize the CDW phase-transition, we employed replica exchange molecular dynamics (REMD) and replica exchange path integral molecular dynamics [87] (PI-REMD), as implemented in the i-PI code. For the 18 × 18 1H-TaS$_2$ supercell, we ran NVT simulations of 26 replicas in parallel that differed in the ensemble temperature. We covered a temperature range between 50 and 200 K. In the PI-REMD simulations, each temperature replica was represented by ten imaginary-time replicas (commonly called "beads" in the ring-polymer representation). This amount of beads proved to be converged within 1 meV/atom for the potential and quantum kinetic energy at the lowest temperature of 50 K. We note that due to the high dimensionality of the system, enhanced by the use of many imaginary-time replicas, the PI-REMD simulations with 26 temperature replicas in this range was not efficient in terms of the frequency of replica swaps, while the REMD simulations were.

References

[1] J. A. Wilson and A. D. Yoffe, *The transition metal dichalcogenides discussion and interpretation of the observed optical, electrical and structural properties*, Adv. Phys. **18**, 193 (1969), doi:10.1080/00018736900101307.

[2] M. Imada, A. Fujimori and Y. Tokura, *Metal-insulator transitions*, Rev. Mod. Phys. **70**, 1039 (1998), doi:10.1103/RevModPhys.70.1039.

[3] K. Rossnagel, *On the origin of charge-density waves in select layered transition-metal dichalcogenides*, J. Phys.: Condens. Matter **23**, 213001 (2011), doi:10.1088/0953-8984/23/21/213001.

[4] D. N. Basov, R. D. Averitt and D. Hsieh, *Towards properties on demand in quantum materials*, Nat. Mater. **16**, 1077 (2017), doi:10.1038/nmat5017.

[5] A. Cavalleri, *Photo-induced superconductivity*, Contemp. Phys. **59**, 31 (2017), doi:10.1080/00107514.2017.1406623.

[6] A. de la Torre, D. M. Kennes, M. Claassen, S. Gerber, J. W. McIver and M. A. Sentef, *Colloquium: Nonthermal pathways to ultrafast control in quantum materials*, Rev. Mod. Phys. **93**, 041002 (2021), doi:10.1103/RevModPhys.93.041002.

[7] D. J. Auerbach, J. C. Tully and A. M. Wodtke, *Chemical dynamics from the gas-phase to surfaces*, Nat. Sci. **1**, e10005 (2021), doi:10.1002/ntls.10005.

[8] B. Slater and A. Michaelides, *Surface premelting of water ice*, Nat. Rev. Chem. **3**, 172 (2019), doi:10.1038/s41570-019-0080-8.

[9] G. Grüner, *Density waves in solids*, CRC Press, Boca Raton, USA, ISBN 9780429501012 (2018), doi:10.1201/9780429501012.

[10] L. Perfetti, P. A. Loukakos, M. Lisowski, U. Bovensiepen, H. Berger, S. Biermann, P. S. Cornaglia, A. Georges and M. Wolf, *Time evolution of the electronic structure of 1T-TaS$_2$ through the insulator-metal transition*, Phys. Rev. Lett. **97**, 067402 (2006), doi:10.1103/PhysRevLett.97.067402.

[11] S. Hellmann et al., *Ultrafast melting of a charge-density wave in the Mott insulator 1T-TaS$_2$*, Phys. Rev. Lett. **105**, 187401 (2010), doi:10.1103/PhysRevLett.105.187401.

[12] M. Eichberger, H. Schäfer, M. Krumova, M. Beyer, J. Demsar, H. Berger, G. Moriena, G. Sciaini and R. J. D. Miller, *Snapshots of cooperative atomic motions in the optical suppression of charge density waves*, Nature **468**, 799 (2010), doi:10.1038/nature09539.

[13] F. Weber et al., *Extended phonon collapse and the origin of the charge-density wave in 2H-NbSe$_2$*, Phys. Rev. Lett. **107**, 107403 (2011), doi:10.1103/PhysRevLett.107.107403.

[14] E. Möhr-Vorobeva et al., *Nonthermal melting of a charge density wave in TiSe$_2$*, Phys. Rev. Lett. **107**, 036403 (2011), doi:10.1103/PhysRevLett.107.036403.

[15] L. Stojchevska, I. Vaskivskyi, T. Mertelj, P. Kusar, D. Svetin, S. Brazovskii and D. Mihailovic, *Ultrafast switching to a stable hidden quantum state in an electronic crystal*, Science **344**, 177 (2014), doi:10.1126/science.1241591.

[16] S. Vogelgesang, G. Storeck, J. G. Horstmann, T. Diekmann, M. Sivis, S. Schramm, K. Rossnagel, S. Schäfer and C. Ropers, *Phase ordering of charge density waves traced by ultrafast low-energy electron diffraction*, Nat. Phys. **14**, 184 (2017), doi:10.1038/nphys4309.

[17] A. Zong et al., *Evidence for topological defects in a photoinduced phase transition*, Nat. Phys. **15**, 27 (2018), doi:10.1038/s41567-018-0311-9.

[18] T. Danz, T. Domröse and C. Ropers, *Ultrafast nanoimaging of the order parameter in a structural phase transition*, Science **371**, 371 (2021), doi:10.1126/science.abd2774.

[19] T. Neupert, M. M. Denner, J.-X. Yin, R. Thomale and M. Z. Hasan, *Charge order and superconductivity in Kagomé materials*, Nat. Phys. **18**, 137 (2021), doi:10.1038/s41567-021-01404-y.

[20] D. J. Hooton, *LI. A new treatment of anharmonicity in lattice thermodynamics: I*, Lond. Edinb. Dublin Philos. Mag. J. Sci. **46**, 422 (1955), doi:10.1080/14786440408520575.

[21] J. M. Bowman, *Self-consistent field energies and wavefunctions for coupled oscillators*, J. Chem. Phys. **68**, 608 (1978), doi:10.1063/1.435782.

[22] P. Souvatzis, O. Eriksson, M. I. Katsnelson and S. P. Rudin, *Entropy driven stabilization of energetically unstable crystal structures explained from first principles theory*, Phys. Rev. Lett. **100**, 095901 (2008), doi:10.1103/PhysRevLett.100.095901.

[23] I. Errea, M. Calandra and F. Mauri, *Anharmonic free energies and phonon dispersions from the stochastic self-consistent harmonic approximation: Application to platinum and palladium hydrides*, Phys. Rev. B **89**, 064302 (2014), doi:10.1103/PhysRevB.89.064302.

[24] R. Bianco, L. Monacelli, M. Calandra, F. Mauri and I. Errea, *Weak dimensionality dependence and dominant role of ionic fluctuations in the charge-density-wave transition of $NbSe_2$*, Phys. Rev. Lett. **125**, 106101 (2020), doi:10.1103/PhysRevLett.125.106101.

[25] C. Falter and M. Selmke, *Renormalization of the dielectric response with applications to effective ion interactions and phonons*, Phys. Rev. B **24**, 586 (1981), doi:10.1103/PhysRevB.24.586.

[26] C. Falter, *A unifying approach to lattice dynamical and electronic properties of solids*, Phys. Rep. **164**, 1 (1988), doi:10.1016/0370-1573(88)90058-0.

[27] A. P. Bartók, M. C. Payne, R. Kondor and G. Csányi, *Gaussian approximation potentials: The accuracy of quantum mechanics, without the electrons*, Phys. Rev. Lett. **104**, 136403 (2010), doi:10.1103/PhysRevLett.104.136403.

[28] J. Finkelstein, J. S. Smith, S. M. Mniszewski, K. Barros, C. F. A. Negre, E. H. Rubensson and A. M. N. Niklasson, *Quantum-based molecular dynamics simulations using tensor cores*, J. Chem. Theory Comput. **17**, 6180 (2021), doi:10.1021/acs.jctc.1c00726.

[29] V. L. Deringer, A. P. Bartók, N. Bernstein, D. M. Wilkins, M. Ceriotti and G. Csányi, *Gaussian process regression for materials and molecules*, Chem. Rev. **121**, 10073 (2021), doi:10.1021/acs.chemrev.1c00022.

[30] Z. Wang, J. Dong, J. Qiu and L. Wang, *All-atom nonadiabatic dynamics simulation of hybrid graphene nanoribbons based on Wannier analysis and machine learning*, ACS Appl. Mater. Interfaces **14**, 22929 (2022), doi:10.1021/acsami.1c22181.

[31] C. Cheng, S. Zhang and G.-W. Chern, *Machine learning for phase ordering dynamics of charge density waves*, Phys. Rev. B **108**, 014301 (2023), doi:10.1103/PhysRevB.108.014301.

[32] M. W. Finnis, A. T. Paxton, D. G. Pettifor, A. P. Sutton and Y. Ohta, *Interatomic forces in transition metals*, Philos. Mag. A **58**, 143 (1988), doi:10.1080/01418618808205180.

[33] C. L. Brooks, *Computer simulation of liquids*, J. Solution Chem. **18**, 99 (1989), doi:10.1007/BF00646086.

[34] C. Z. Wang, C. T. Chan and K. M. Ho, *Empirical tight-binding force model for molecular-dynamics simulation of Si*, Phys. Rev. B **39**, 8586 (1989), doi:10.1103/PhysRevB.39.8586.

[35] L. Goodwin, A. J. Skinner and D. G. Pettifor, *Generating transferable tight-binding parameters: Application to silicon*, Europhys. Lett. **9**, 701 (1989), doi:10.1209/0295-5075/9/7/015.

[36] W. Matthew C. Foulkes and R. Haydock, *Tight-binding models and density-functional theory*, Phys. Rev. B **39**, 12520 (1989), doi:10.1103/PhysRevB.39.12520.

[37] O. F. Sankey and D. J. Niklewski, *Ab initio multicenter tight-binding model for molecular-dynamics simulations and other applications in covalent systems*, Phys. Rev. B **40**, 3979 (1989), doi:10.1103/PhysRevB.40.3979.

[38] K. Laasonen and R. M. Nieminen, *Molecular dynamics using the tight-binding approximation*, J. Phys.: Condens. Matter **2**, 1509 (1990), doi:10.1088/0953-8984/2/6/010.

[39] R. Virkkunen, K. Laasonen and R. M. Nieminen, *Molecular dynamics using the tight-binding approximation: Application to liquid silicon*, J. Phys.: Condens. Matter **3**, 7455 (1991), doi:10.1088/0953-8984/3/38/017.

[40] C. Z. Wang, C. T. Chan and K. M. Ho, *Tight-binding molecular-dynamics study of liquid Si*, Phys. Rev. B **45**, 12227 (1992), doi:10.1103/PhysRevB.45.12227.

[41] C. Molteni, L. Colombo and L. Miglio, *Structural properties of liquid and amorphous GaAs by tight-binding molecular dynamics*, Europhys. Lett. **24**, 659 (1993), doi:10.1209/0295-5075/24/8/007.

[42] D. Porezag, T. Frauenheim, T. Köhler, G. Seifert and R. Kaschner, *Construction of tight-binding-like potentials on the basis of density-functional theory: Application to carbon*, Phys. Rev. B **51**, 12947 (1995), doi:10.1103/PhysRevB.51.12947.

[43] Y. P. Feng, C. K. Ong, H. C. Poon and D. Tománek, *Tight-binding molecular dynamics simulations of semiconductor alloys: Clusters, surfaces, and defects*, J. Phys.: Condens. Matter **9**, 4345 (1997), doi:10.1088/0953-8984/9/21/003.

[44] M. Elstner, D. Porezag, G. Jungnickel, J. Elsner, M. Haugk, T. Frauenheim, S. Suhai and G. Seifert, *Self-consistent-charge density-functional tight-binding method for simulations of complex materials properties*, Phys. Rev. B **58**, 7260 (1998), doi:10.1103/PhysRevB.58.7260.

[45] C.-C. Fu and M. Weissmann, *Tight-binding molecular-dynamics study of amorphous carbon deposits over silicon surfaces*, Phys. Rev. B **60**, 2762 (1999), doi:10.1103/PhysRevB.60.2762.

[46] B. Aradi, B. Hourahine and T. Frauenheim, *DFTB+, a sparse matrix-based implementation of the DFTB method*, J. Phys. Chem. A **111**, 5678 (2007), doi:10.1021/jp070186p.

[47] J. P. Lewis et al., *Advances and applications in the FIREBAL ab initio tight-binding molecular-dynamics formalism*, Physica Status Solidi (b) **248**, 1989 (2011), doi:10.1002/pssb.201147259.

[48] P. García-Fernández, J. C. Wojdeł, J. Íñiguez and J. Junquera, *Second-principles method for materials simulations including electron and lattice degrees of freedom*, Phys. Rev. B **93**, 195137 (2016), doi:10.1103/PhysRevB.93.195137.

[49] Z. H. He, X. B. Ye and B. C. Pan, *Linear scaling algorithm for tight-binding molecular dynamics simulations*, J. Chem. Phys. **150**, 114107 (2019), doi:10.1063/1.5088918.

[50] Y. Nishimura and H. Nakai, *Dcdftbmd: Divide-and-conquer density functional tight-binding program for huge-system quantum mechanical molecular dynamics simulations*, J Comput Chem **40**, 1538 (2019), doi:10.1002/jcc.25804.

[51] B. Hourahine et al., *DFTB+, a software package for efficient approximate density functional theory based atomistic simulations*, J. Chem. Phys. **152**, 124101 (2020), doi:10.1063/1.5143190.

[52] A. M. N. Niklasson, *Density-matrix based extended Lagrangian Born-Oppenheimer molecular dynamics*, J. Chem. Theory Comput. **16**, 3628 (2020), doi:10.1021/acs.jctc.0c00264.

[53] L. Zhang, B. Onat, G. Dusson, A. McSloy, G. Anand, R. J. Maurer, C. Ortner and J. R. Kermode, *Equivariant analytical mapping of first principles Hamiltonians to accurate and transferable materials models*, npj Comput. Mater. **8**, 158 (2022), doi:10.1038/s41524-022-00843-2.

[54] P. Hohenberg and W. Kohn, *Inhomogeneous electron gas*, Phys. Rev. **136**, B864 (1964), doi:10.1103/PhysRev.136.B864.

[55] F. Aryasetiawan and F. Nilsson, *Downfolding methods in many-electron theory*, AIP Publishing, College Park, USA, ISBN 9780735422469 (2022), doi:10.1063/9780735422490.

[56] T. Fujiwara, S. Yamamoto and Y. Ishii, *Generalization of the iterative perturbation theory and metal-insulator transition in multi-orbital Hubbard bands*, J. Phys. Soc. Jpn. **72**, 777 (2003), doi:10.1143/JPSJ.72.777.

[57] F. Aryasetiawan, M. Imada, A. Georges, G. Kotliar, S. Biermann and A. I. Lichtenstein, *Frequency-dependent local interactions and low-energy effective models from electronic structure calculations*, Phys. Rev. B **70**, 195104 (2004), doi:10.1103/PhysRevB.70.195104.

[58] F. Aryasetiawan, K. Karlsson, O. Jepsen and U. Schönberger, *Calculations of Hubbard U from first-principles*, Phys. Rev. B **74**, 125106 (2006), doi:10.1103/PhysRevB.74.125106.

[59] K. Nakamura, R. Arita and M. Imada, *Ab initio derivation of low-energy model for iron-based superconductors LaFeAsO and LaFePO*, J. Phys. Soc. Jpn. **77**, 093711 (2008), doi:10.1143/JPSJ.77.093711.

[60] Y. Nohara, S. Yamamoto and T. Fujiwara, *Electronic structure of perovskite-type transition metal oxides $LaMO_3$ ($M = Ti \sim Cu$) by $U + GW$ approximation*, Phys. Rev. B **79**, 195110 (2009), doi:10.1103/PhysRevB.79.195110.

[61] K. Nakamura, Y. Yoshimoto, T. Kosugi, R. Arita and M. Imada, *Ab initio derivation of low-energy model for κ-ET type organic conductors*, J. Phys. Soc. Jpn. **78**, 083710 (2009), doi:10.1143/JPSJ.78.083710.

[62] K. Nakamura, Y. Nohara, Y. Yosimoto and Y. Nomura, *Ab initio GW plus cumulant calculation for isolated band systems: Application to organic conductor $(TMTSF)_2PF_6$ and transition-metal oxide $SrVO_3$*, Phys. Rev. B **93**, 085124 (2016), doi:10.1103/PhysRevB.93.085124.

[63] G. Giovannetti, M. Casula, P. Werner, F. Mauri and M. Capone, *Downfolding electron-phonon Hamiltonians from ab initio calculations: Application to K_3 picene*, Phys. Rev. B **90**, 115435 (2014), doi:10.1103/PhysRevB.90.115435.

[64] Y. Nomura and R. Arita, *Ab initio downfolding for electron-phonon-coupled systems: Constrained density-functional perturbation theory*, Phys. Rev. B **92**, 245108 (2015), doi:10.1103/PhysRevB.92.245108.

[65] Y. Nomura, S. Sakai, M. Capone and R. Arita, *Exotic s -wave superconductivity in alkali-doped fullerides*, J. Phys.: Condens. Matter **28**, 153001 (2016), doi:10.1088/0953-8984/28/15/153001.

[66] J. Berges, E. G. C. P. van Loon, A. Schobert, M. Rösner and T. O. Wehling, *Ab initio phonon self-energies and fluctuation diagnostics of phonon anomalies: Lattice instabilities from Dirac pseudospin physics in transition metal dichalcogenides*, Phys. Rev. B **101**, 155107 (2020), doi:10.1103/PhysRevB.101.155107.

[67] E. G. C. P. van Loon, J. Berges and T. O. Wehling, *Downfolding approaches to electron-ion coupling: Constrained density-functional perturbation theory for molecules*, Phys. Rev. B **103**, 205103 (2021), doi:10.1103/PhysRevB.103.205103.

[68] M. Kinza and C. Honerkamp, *Low-energy effective interactions beyond the constrained random-phase approximation by the functional renormalization group*, Phys. Rev. B **92**, 045113 (2015), doi:10.1103/PhysRevB.92.045113.

[69] C. Honerkamp, *Efficient vertex parametrization for the constrained functional renormalization group for effective low-energy interactions in multiband systems*, Phys. Rev. B **98**, 155132 (2018), doi:10.1103/PhysRevB.98.155132.

[70] X.-J. Han, P. Werner and C. Honerkamp, *Investigation of the effective interactions for the Emery model by the constrained random-phase approximation and constrained functional renormalization group*, Phys. Rev. B **103**, 125130 (2021), doi:10.1103/PhysRevB.103.125130.

[71] M. Born and R. Oppenheimer, *Zur Quantentheorie der Molekeln*, Ann. Phys. **389**, 457 (1927), doi:10.1002/andp.19273892002.

[72] Y. Nomura et al., *Effective on-site interaction for dynamical mean-field theory*, Phys. Rev. B **86**, 085117 (2012), doi:10.1103/PhysRevB.86.085117.

[73] M. Calandra, G. Profeta and F. Mauri, *Adiabatic and nonadiabatic phonon dispersion in a Wannier function approach*, Phys. Rev. B **82**, 165111 (2010), doi:10.1103/PhysRevB.82.165111.

[74] J. Berges, A. Schobert, E. G. C. P. van Loon, M. Rösner and T. O. Wehling, *elphmod: Python modules for electron-phonon models*, Zenodo (2017), doi:10.5281/zenodo.5919991.

[75] F. Giustino, M. L. Cohen and S. G. Louie, *Electron-phonon interaction using Wannier functions*, Phys. Rev. B **76**, 165108 (2007), doi:10.1103/PhysRevB.76.165108.

[76] J. Berges, N. Girotto, T. Wehling, N. Marzari and S. Poncé, *Phonon self-energy corrections: To screen, or not to screen*, Phys. Rev. X **13**, 041009 (2023), doi:10.1103/PhysRevX.13.041009.

[77] O. R. Albertini, A. Y. Liu and M. Calandra, *Effect of electron doping on lattice instabilities in single-layer 1H-TaS$_2$*, Phys. Rev. B **95**, 235121 (2017), doi:10.1103/PhysRevB.95.235121.

[78] D. C. Miller, S. D. Mahanti and P. M. Duxbury, *Charge density wave states in tantalum dichalcogenides*, Phys. Rev. B **97**, 045133 (2018), doi:10.1103/PhysRevB.97.045133.

[79] H. M. Lefcochilos-Fogelquist, O. R. Albertini and A. Y. Liu, *Substrate-induced suppression of charge density wave phase in monolayer 1H-TaS₂ on Au(111)*, Phys. Rev. B **99**, 174113 (2019), doi:10.1103/PhysRevB.99.174113.

[80] W. H. Sio, C. Verdi, S. Poncé and F. Giustino, *Ab initio theory of polarons: Formalism and applications*, Phys. Rev. B **99**, 235139 (2019), doi:10.1103/PhysRevB.99.235139.

[81] W. H. Sio, C. Verdi, S. Poncé and F. Giustino, *Polarons from first principles, without supercells*, Phys. Rev. Lett. **122**, 246403 (2019), doi:10.1103/PhysRevLett.122.246403.

[82] A. Klein, S. Tiefenbacher, V. Eyert, C. Pettenkofer and W. Jaegermann, *Electronic band structure of single-crystal and single-layer WS₂: Influence of interlayer van der Waals interactions*, Phys. Rev. B **64**, 205416 (2001), doi:10.1103/PhysRevB.64.205416.

[83] P. Giannozzi et al., *QUANTUM ESPRESSO: A modular and open-source software project for quantum simulations of materials*, J. Phys.: Condens. Matter **21**, 395502 (2009), doi:10.1088/0953-8984/21/39/395502.

[84] P. Giannozzi et al., *Advanced capabilities for materials modelling with Quantum ESPRESSO*, J. Phys.: Condens. Matter **29**, 465901 (2017), doi:10.1088/1361-648X/aa8f79.

[85] C. R. Harris et al., *Array programming with NumPy*, Nature **585**, 357 (2020), doi:10.1038/s41586-020-2649-2.

[86] P. Virtanen et al., *SciPy 1.0: Fundamental algorithms for scientific computing in Python*, Nat. Methods **17**, 261 (2020), doi:10.1038/s41592-019-0686-2.

[87] V. Kapil et al., *i-PI 2.0: A universal force engine for advanced molecular simulations*, Comput. Phys. Commun. **236**, 214 (2019), doi:10.1016/j.cpc.2018.09.020.

[88] Y. Zheng, X. Jiang, X.-X. Xue, X. Yao, J. Zeng, K.-Q. Chen, E. Wang and Y. Feng, *Nuclear quantum effects on the charge-density wave transition in NbX₂ (X = S, Se)*, Nano Lett. **22**, 1858 (2022), doi:10.1021/acs.nanolett.1c04015.

[89] J. Hall et al., *Environmental control of charge density wave order in monolayer 2H-TaS₂*, ACS Nano **13**, 10210 (2019), doi:10.1021/acsnano.9b03419.

[90] J. P. Tidman, O. Singh, A. E. Curzon and R. F. Frindt, *The phase transition in 2H-TaS₂ at 75 K*, Philos. Mag.: J. Theor. Exp. Appl. Phys. **30**, 1191 (1974), doi:10.1080/14786437408207274.

[91] G. A. Scholz, O. Singh, R. F. Frindt and A. E. Curzon, *Charge density wave commensurability in 2H-TaS₂ and AgₓTaS₂*, Solid State Commun. **44**, 1455 (1982), doi:10.1016/0038-1098(82)90030-8.

[92] S. Sugai, *Lattice vibrations in the charge-density-wave states of layered transition metal dichalcogenides*, Phys. Status Solidi B **129**, 13 (1985), doi:10.1002/pssb.2221290103.

[93] D. Lin et al., *Patterns and driving forces of dimensionality-dependent charge density waves in 2H-type transition metal dichalcogenides*, Nat. Commun. **11**, 2406 (2020), doi:10.1038/s41467-020-15715-w.

[94] X.-M. Zhao et al., *Pressure tuning of the charge density wave and superconductivity in 2H-TaS₂*, Phys. Rev. B **101**, 134506 (2020), doi:10.1103/PhysRevB.101.134506.

[95] M. Lee, M. Šiškins, S. Mañas-Valero, E. Coronado, P. G. Steeneken and H. S. J. van der Zant, *Study of charge density waves in suspended 2H-TaS₂ and 2H-TaSe₂ by nanomechanical resonance*, Appl. Phys. Lett. **118**, 193105 (2021), doi:10.1063/5.0051112.

[96] F. Karsai, M. Engel, E. Flage-Larsen and G. Kresse, *Electron-phonon coupling in semiconductors within the GW approximation*, New J. Phys. **20**, 123008 (2018), doi:10.1088/1367-2630/aaf53f.

[97] S. Wall et al., *Ultrafast disordering of vanadium dimers in photoexcited VO₂*, Science **362**, 572 (2018), doi:10.1126/science.aau3873.

[98] A. Schobert, J. Berges, E. van Loon, M. Sentef, S. Brener, M. Rossi and T. O. Wehling, *Data of the publication "Ab initio electron-lattice downfolding: Potential energy landscapes, anharmonicity, and molecular dynamics in charge density wave materials"*, Zenodo (2023), doi:10.5281/zenodo.10514203.

[99] M. Rösner, E. Şaşıoğlu, C. Friedrich, S. Blügel and T. O. Wehling, *Wannier function approach to realistic Coulomb interactions in layered materials and heterostructures*, Phys. Rev. B **92**, 085102 (2015), doi:10.1103/PhysRevB.92.085102.

[100] T. Matsubara, *A new approach to quantum-statistical mechanics*, Prog. Theor. Phys. **14**, 351 (1955), doi:10.1143/PTP.14.351.

[101] S. Baroni, S. de Gironcoli, A. Dal Corso and P. Giannozzi, *Phonons and related crystal properties from density-functional perturbation theory*, Rev. Mod. Phys. **73**, 515 (2001), doi:10.1103/RevModPhys.73.515.

[102] A. A. Mostofi, J. R. Yates, G. Pizzi, Y.-S. Lee, I. Souza, D. Vanderbilt and N. Marzari, *An updated version of wannier90: A tool for obtaining maximally-localised Wannier functions*, Comput. Phys. Commun. **185**, 2309 (2014), doi:10.1016/j.cpc.2014.05.003.

[103] J. Noffsinger, F. Giustino, B. D. Malone, C.-H. Park, S. G. Louie and M. L. Cohen, *EPW: A program for calculating the electron-phonon coupling using maximally localized Wannier functions*, Comput. Phys. Commun. **181**, 2140 (2010), doi:10.1016/j.cpc.2010.08.027.

[104] S. Poncé, E. R. Margine, C. Verdi and F. Giustino, *EPW: Electron-phonon coupling, transport and superconducting properties using maximally localized Wannier functions*, Comput. Phys. Commun. **209**, 116 (2016), doi:10.1016/j.cpc.2016.07.028.

[105] H. Lee et al., *Electron-phonon physics from first principles using the EPW code*, npj Comput. Mater. **9**, 156 (2023), doi:10.1038/s41524-023-01107-3.

[106] K. Nakamura, Y. Yoshimoto, Y. Nomura, T. Tadano, M. Kawamura, T. Kosugi, K. Yoshimi, T. Misawa and Y. Motoyama, *RESPACK: An ab initio tool for derivation of effective low-energy model of material*, Comput. Phys. Commun. **261**, 107781 (2021), doi:10.1016/j.cpc.2020.107781.

[107] S. Goedecker, M. Teter and J. Hutter, *Separable dual-space Gaussian pseudopotentials*, Phys. Rev. B **54**, 1703 (1996), doi:10.1103/PhysRevB.54.1703.

[108] C. Hartwigsen, S. Goedecker and J. Hutter, *Relativistic separable dual-space Gaussian pseudopotentials from H to Rn*, Phys. Rev. B **58**, 3641 (1998), doi:10.1103/PhysRevB.58.3641.

[109] D. Vanderbilt, *Soft self-consistent pseudopotentials in a generalized eigenvalue formalism*, Phys. Rev. B **41**, 7892 (1990), doi:10.1103/PhysRevB.41.7892.

[110] G. Prandini, A. Marrazzo, I. E. Castelli, N. Mounet and N. Marzari, *Precision and efficiency in solid-state pseudopotential calculations*, npj Comput. Mater. **4**, 72 (2018), doi:10.1038/s41524-018-0127-2.

[111] G. Prandini, A. Marrazzo, I. E. Castelli, N. Mounet, E. Passaro and N. Marzari, *A standard solid state pseudopotentials (SSSP) library optimized for precision and efficiency*, Mater. Cloud Arch. **76** (2021), doi:10.24435/materialscloud:rz-77.

[112] D. R. Hamann, *Optimized norm-conserving Vanderbilt pseudopotentials*, Phys. Rev. B **88**, 085117 (2013), doi:10.1103/PhysRevB.88.085117.

[113] M. J. van Setten, M. Giantomassi, E. Bousquet, M. J. Verstraete, D. R. Hamann, X. Gonze and G.-M. Rignanese, *The PseudoDojo: Training and grading a 85 element optimized norm-conserving pseudopotential table*, Comput. Phys. Commun. **226**, 39 (2018), doi:10.1016/j.cpc.2018.01.012.

[114] J. P. Perdew, K. Burke and M. Ernzerhof, *Generalized gradient approximation made simple*, Phys. Rev. Lett. **77**, 3865 (1996), doi:10.1103/PhysRevLett.77.3865.